

Convection of Low-Energy Fluid by Secondary Flow in a Low Speed Centrifugal Compressor Impeller

Huiqi Ruan¹, Huanxin Lai¹

¹School of Mechanical and Power Engineering,
East China University of Science and Technology
130 Meilong Road, Shanghai, Xuhui District, Shanghai, P.R. China
huiqiR0@163.com; hlai@ecust.edu.cn

Abstract - In this paper, RANS simulation of the three-dimensional flow in the impeller of the NASA low speed centrifugal compressor (LSCC) is carried out. The two-equation k- ϵ model combined with the enhanced wall function is employed for turbulence closure. Attentions are paid to the convection of the low-energy fluid by secondary flow in a series of cross-sections along the flow passage in the impeller. The distribution and development of the tip leakage vortex (TLV) and the scraping vortex (SV) near the casing are visualized by the sectional spin lines, while the migration of the passage vortex (PV) is shown by the sectional streamlines. The dissipative function, which is used to analyze the occurrence of flow loss, shows that the peak of energy dissipation is concentrated in the wall surface, and in the area where the leakage vortex occurs. The scraping vortex appears in area which is occupied by low-energy fluid. This paper provides a basis for exploring energy loss caused by the non-uniform flow inside the LSCC impeller.

Keywords: centrifugal compressor, secondary flow, tip leakage vortex, scraping vortex, passage vortex

1. Introduction

Centrifugal compressors are used for increasing pressure in process engineering. The secondary flow is a known factor of energy loss for in compressors, which is caused by the imbalance of local static pressure field and fluid kinetic energy, resulting in a transverse flow deviating from the mainstream direction [1]. The low-energy fluid translated by the secondary flow can further result in non-uniform distribution of flow field in cross-sections of the flow path [2]. Such convection process is crucial to the flow efficiency and need to be carefully studied.

Researchers explored the flow characteristics in the impeller through experiments and simulations. Aerodynamic probes were widely used to measure the flow inside the impeller [3]. Back in the 1980s, Johnson [4] had established the relationship between the reduced static pressure and the rotary stagnation pressure with the formation of the secondary flow by measuring different flow cross-sections inside the Ghost impeller, and observed the wake flow occurring in the corner between the casing and suction surface. Up to now, the method of measuring flow field in the impeller has been fully developed.

In terms of simulation, Kang [5] verified secondary flow is driven by the reduced static pressure by analyzing a centrifugal impeller with high pressure ratio. Xi [6] obtained the three-dimensional velocity field and performance curve inside NASA LSCC [7] under a wide working condition by simulation, and proved that CFD method can reflect the three-dimensional flow characteristics inside the impeller in detail. Ghenaïet [8] compared the prediction method and inducement of compressor stall of two different compressors.

A review of relevant literature on centrifugal compressors shows that the current experimental and numerical simulation methods have allowed basic information of the flow field inside the impeller. However, the causes for the non-uniform flow isn't fully understood. This paper then selects NASA LSCC as the research object, and results in a numerical analysis, focusing on the convection of low-energy fluids in the internal flow field of the impeller and the secondary flow characteristics.

2. Numerical Models

2.1. Flow Passage and Grid Distribution

The Structure and performance parameters of NASA LSCC channel model established in this paper are derived from the experimental report published by NASA in 1995 [7] which contained detailed information of pressure, velocity and temperature field. The impeller of LSCC is consist of 20 full blades with a backsweep angle of 55°. The inlet diameter is

870mm and the exit diameter is 1524mm. The clearance between the blade tip and the shroud is a constant 2.54mm along the impeller. The impeller takes air in from the axial direction and exhausts in the radial direction with a design rotating speed at 1862rpm.

Fig. 1 shows the geometric model and grid distribution of the computational domain in the single channel of the impeller. The two sides of the flow channel which is colored in blue are the pressure surface and the suction surface of two adjacent blades, and the tip clearance area which is colored in red is arranged on the pressure side. Inlet passage, blade passage, tip clearance, and diffuser passage are all built as separate blocks to build a hexahedral mesh. The leading edge of the blade is located at $z=0$. In the NASA experimental report, the impeller inlet aerodynamic survey data were measured at the $z=-203.73\text{mm}$ section. Therefore, this measuring section is taken as the inlet boundary of the computational domain, and the diffuser outlet is set as the outlet boundary.

RANS simulation is carried out to reflect the three-dimensional flow in the impeller of the NASA LSCC. Considering the accuracy of high Reynolds number flow simulation [7], the two-equation $k-\epsilon$ model combined with the enhanced wall function is employed for turbulence closure, and the central difference is selected by the spatial discretization scheme. In order to meet the requirements of enhanced wall function, the height of near wall grid is densified to 0.02mm to ensure $y^+ < 5$. Since LSCC has a tip speed of $U_t = 153\text{m/s}$ which is greater than 0.3 times of the sound speed, the ideal gas (air) is selected as the working medium to reproduce the compressibility. The inlet boundary condition is set by the measured aerodynamic survey data, and the mass flow boundary condition are adopted at the outlet with a design flow rate of 30kg/s. In addition, the inlet temperature is set at 288.15k, the circumferential section is set as the periodic boundary, and the other walls are set as the non slip adiabatic wall.

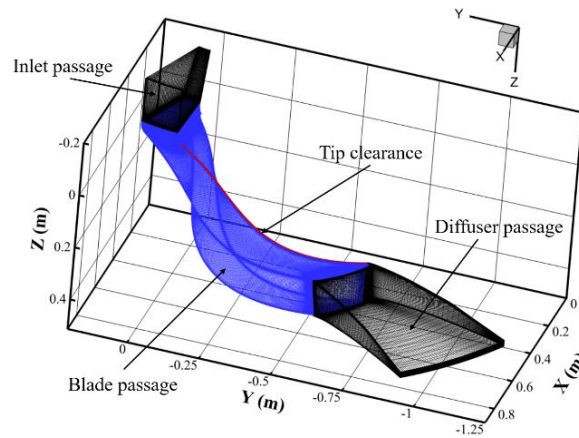


Fig. 1: Grid distribution of a single channel

2.2. Grid Independence

Five grid topologies, whose distribution is shown in Table 1, are adopted in this study to delineate the grid dependency. The difference of the inlet and outlet pressure ratio (P_o/P_i) and adiabatic efficiency (η_{ad}) of a single channel were compared in Fig. 2 with the changing of mesh number (N). It can be observed that when the mesh number reaches 3 million, the calculation results have met the requirements of grid independence. Therefore, the grid node distribution of the adopted calculation model is shown in the No. 5 grid in Table 1. Lots of the grids are arranged in the blade channel to ensure the reliability of the simulation results inside the impeller.

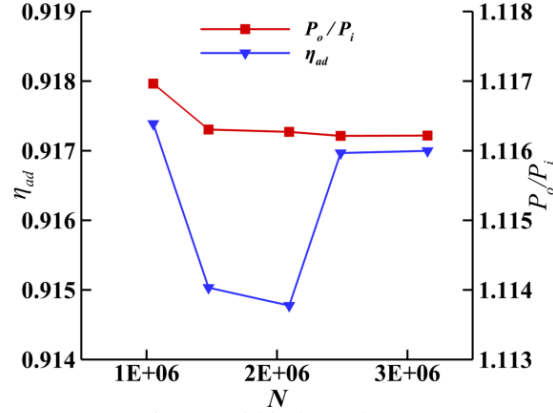


Fig. 2: Grid independence

Table 1: Grid Node Distribution

Grid	Spread	Upstream	Blade	Downstream	Height	N (10 ⁶)
1	37	61	257	49	65	1.05
2	41	61	309	49	73	1.47
3	45	61	443	53	73	2.09
4	45	61	517	53	77	2.49
5	45	61	585	53	89	3.15

3. Results And Discussion

3.1. Experimental Validations

To verify the simulation results, the reduced static pressure on the blade surface and the three-dimensional velocity field in different blade height are compared. The reduced static pressure P_r is a physical quantity used to express the static pressure distribution inside the impeller without the affect of centrifugal force. Definition of P_r in compressible condition is shown in Eqs. (1), where P is the static pressure and ω is the rotation velocity, r is the radial distance, C_p is the isobaric heat capacity, and W is the relative velocity.

$$P_r = P / \left[1 + \frac{\omega^2 r^2 / 2C_p}{T^*} \right]^{\frac{\gamma}{\gamma-1}} ; T^* = T + \frac{W^2 - \omega^2 r^2}{2C_p} \quad (1)$$

Fig. 3 shows the comparison between simulation and measured values of the reduced static pressure on the blade surface at different heights. In this plot, the abscissa is the normalized meridional arc length, the ordinate is the reduced static pressure normalized by reference pressure, which value is $P_{std} = 101325\text{pa}$ and S represents the normalized position in the blade height direction. It can be seen from the figure that the results between simulation and experiment depict a fairly good agreement. Although the simulation value at the blade trailing edge is slightly lower than the experimental value, it still shows a consistent change trend, indicating that the pressure field's characteristics inside the impeller are successfully reproduced by simulation.

In the experiment report by NASA, a series of laser probe were arranged in the position shown in Fig. 4 (d) to obtain the three-dimensional velocity field information inside the impeller. Fig. 4 compares the rotating velocity in the radial direction between experimental and simulation results in three sections from the impeller inlet to the outlet ((a) inlet section $J = 51$, (b) middle section $J = 118$, (c) near outlet section $J = 165$) under the design flow. According to the figure, abscissa is the normalized spanwise span, and ordinate is the radial relative velocity normalized by blade tip velocity $U_t = 153\text{m/s}$. The simulated relative velocity from the impeller channel is basically consistent with the measured value, but there are some errors in the velocity distribution at the blade top of some sections and the blade walls on both sides, which may be due to the difficulty of a laser velocimeter to measure the flow near the wall. Combined with the comparison of blade surface pressure, it is proved that the simulation results in this paper can effectively reflect three-dimensional flow in the test impeller.

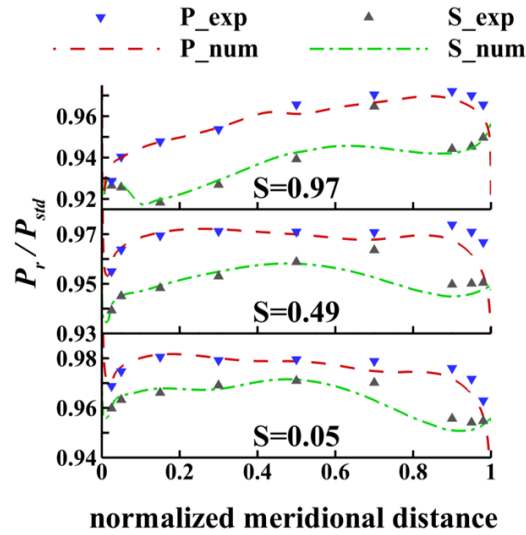


Fig. 3: Reduced static pressure distribution

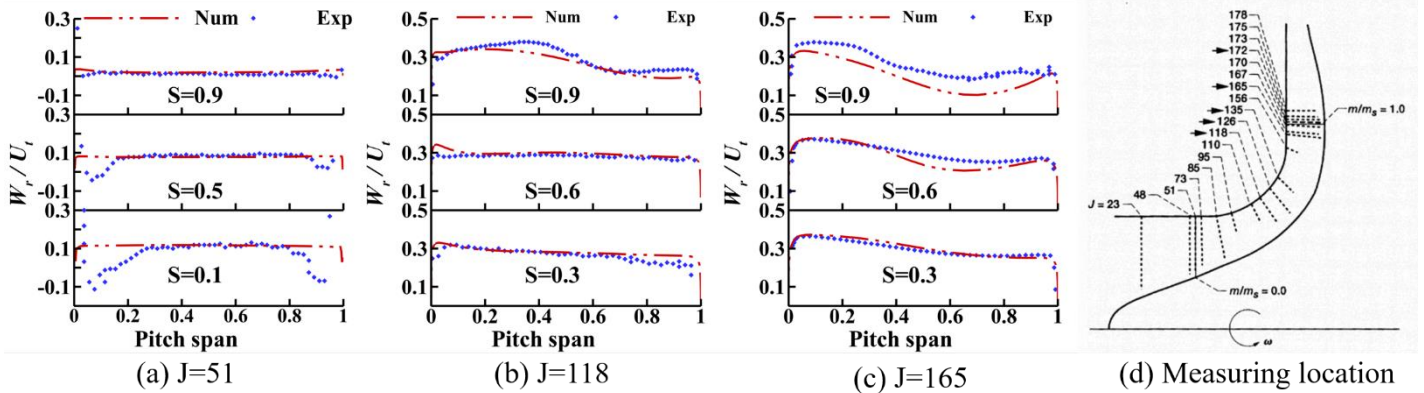


Fig. 4: Velocity distribution in blade height direction

3.2. Generation of the Vortex System near Casing

Second flow in the turbomachinery is the fluid moving away from the main flow direction in the ternary flow. The convection and accumulation of low-energy fluid is the key reasons for a secondary flow generation. Since the total energy in fluid motion is composed of pressure and velocity energy, furthermore, in the blade passage of a low-speed compressor, pressure variation is relatively low, so the fluid with lower velocity energy can be considered as low-energy fluid. Moreover, the absolute velocity of the fluid contains the part generated by the moving together with the impeller, so this paper uses the relative velocity as a reference to the measurement of the fluid velocity energy.

The centerline's normal plane of the blade passage is selected as flow pass section. The sectional spin lines and streamline is used to describe the secondary flow in the impeller. Fig. 5 shows the location of center line of the blade passage and the pass flow sections. The blue line in solid color indicates the center line of the blade channel. By establishing the normal plane of the centerline, the pass flow section is achieved at 10%, 20%, 30%, 40%, 50%, 60%, 70%, 80% and 85% of the channel. Clear passage vortex can be seen in black sections (section A, B, C, D and E), while red sections (section I, II, III and IV) are used to display the distribution of scraping vortex and leakage vortex in the blade tip area.

The vortex system inside a centrifugal impeller always has complex three-dimensional structures, so it's difficult to observe the complete vortex system in the flow section, especially for small-scale vortices such as leakage vortex and scraping vortex locating in the blade tip area. When the normal direction of the selected flow

cross-section disengages from the direction of the vortex core connection line, it's even disable to identify such vortices through the cross-sectional streamlines. In this case, a sectional spin line is introduced to deal with it referring to Zhu [9] and Kang [10].

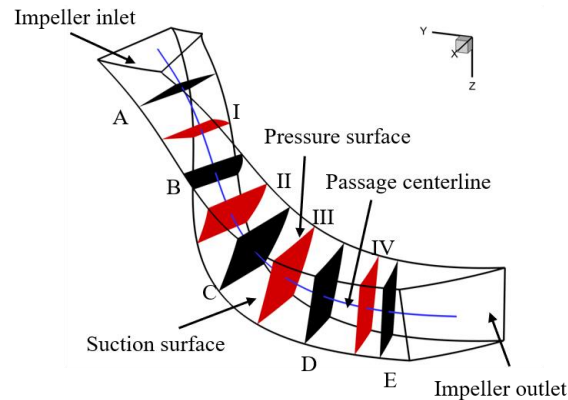


Fig. 5: Location of the pass flow section

$$\vec{S} = (\vec{\omega} \times \vec{V}) \times \vec{n} \quad (2)$$

The definition of section rotation vector \vec{S} is shown in Eqs. (2) where $\vec{\omega}$ is vorticity, \vec{V} is velocity, and \vec{n} is unit normal vector of the selected section. The integral curve of \vec{S} on the plane is sectional spin line. This method uses a vector field constructed by vorticity and velocity, which contains more abundant flow field information than a three-dimensional velocity field. Furthermore, since the normal vector has modified the vector field, the vortex system structure displayed in the sectional spin line won't be deformed due to different observation sections' influences. Therefore, it's an ideal way for the observation of scraping vortex and leakage vortex.

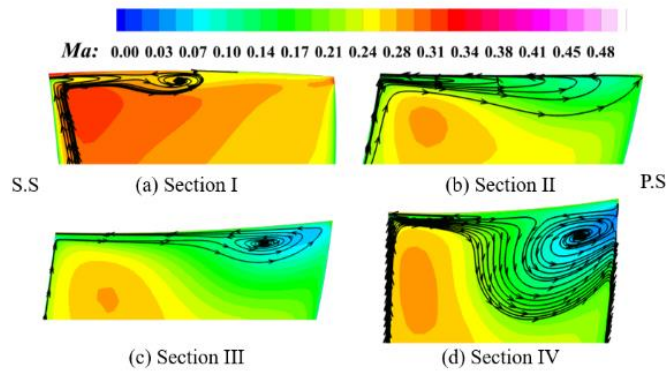


Fig. 6: Sectional spin lines and contours of relative Ma

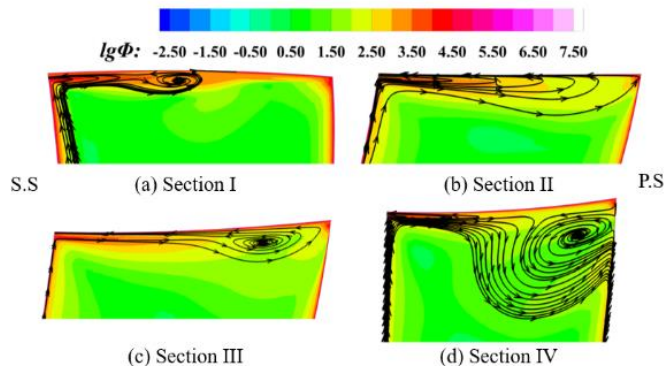


Fig. 7: Sectional spin lines and contours of logarithmic dissipation function

Fig. 6 shows the sectional spin lines and contours of relative Mach number near the casing under the design condition at the (a) 20% (b) 40% (c) 60% (d) 70% flow section. In the figure, it's able to identify the development of leakage vortex and scraping vortex in the near inlet section, the middle section and the near outlet section along the flow channel in the blade top area. In section I, a high-speed fluid at the inlet of the impeller is concentrated in the suction side casing corner area. Under the relative movement between blade and casing, low-energy fluid near the casing is convected from the pressure side through the tip clearance to the suction side. Due to the viscosity of the wall, the fluid on the casing surface has a clockwise movement trend relative to the mainstream direction, and the leakage flow moves in the counterclockwise direction of the mainstream. The intersection of the two fluids forms a counterclockwise leakage vortex. When the flow is transported along the direction of the passage, the low-energy fluid gradually begins to converge in the pressure side hub corner. It's seen from section II that when flow reaches 40% of the flow direction, the edge of leakage vortex has touched the pressure side and doesn't show an obvious vortex core any longer. The geometric bending of the blade to the radial section gradually increases as the flow begins to reach section III, resulting in the raising of the circumferential speed. This way, it can be seen that the low-energy fluid flowing to the pressure surface starts to converge again into vortex under the scraping action of the blade. Finally, gas reaches the section IV near the impeller's outlet, low-energy fluid area in the pressure side hub corner area gradually expands, and the volume of scraping vortex further increases, which begins to affect the flow in the mainstream area.

To study the influence of various vortex systems on flow, the dissipation function Φ is introduced, which is the power of viscous stress on unit volume of fluid during fluid deformation, transforming mechanical energy into internal energy and causing energy loss. Since the calculated value of dissipation function ranges from 10^2 to 10^8 , logarithm of Φ allows a intuitive distribution of dissipation function. The section spin lines and logarithmic contours of the dissipation function under the design condition as shown in Fig. 7. With the figure, the high dissipation area is mainly distributed on the wall and where a leakage vortex appears. The high dissipation near the wall is based on the velocity gradient between the boundary layer and the main stream. During the fluid velocity decreases from the average velocity of the main stream to 0, the shear stress from the wall causes energy loss. As well as the convergence of leakage vortices, the velocity of low-energy fluid convected from the pressure side across the blade to the suction side is much lower than the velocity of high-speed fluid collected in the corner between suction side the casing, thus the velocity gradient between the two brings high dissipation. On the contrary, although lots of low-energy fluids are also found in scraping vortices, it's true from Fig. 6 that there's no sudden change in velocity, so there is no high dissipation of fluid energy.

3.3. Vortex System Development of Blade Passage

The complex structure of centrifugal impeller is an important factor to passage vortex. This secondary flow in general has three generation mechanisms: (1) the flow itself is rotary or the channel has complex geometric turning; (2) the flow channel has a tendency to convergence or divergence along the flow direction; (3) the turning of the runner changes the flow direction. The geometry of the blade passage in a centrifugal impeller can be considered as a curved rectangular channel with a 90° rotation. Two types of vortex structures are mainly generated along the flow pass, which is driven by a) stress and b) pressure. The stress driven secondary flow is characterized by passing to the corner of the pipe along the angle bisector, generally occupying a quarter of the quadrant of the pipe. While the pressure driven secondary flow is composed of two counter rotating vortices, which flow from the middle plane of the pipe to the outer wall along the bottom side, and taking back to the middle plane along the top side [11].

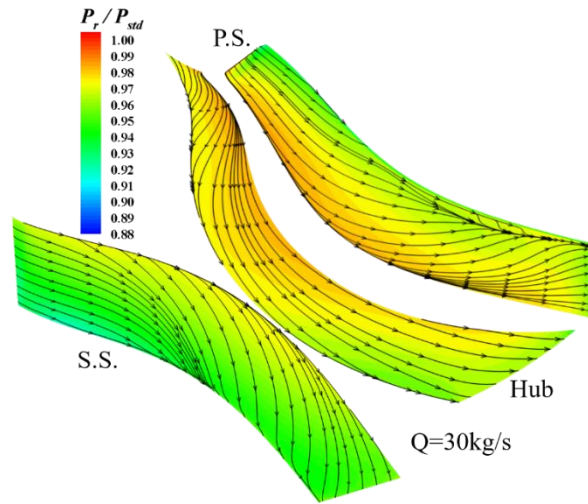


Fig. 8: Limiting streamlines and contours of reduced static pressure

The limiting streamlines and contours of normalized reduced static pressure on the pressure side, suction side and hub surface under design condition are shown in Fig. 8, whereas displaying the convection characteristics of low-energy fluid in the boundary layer of impeller surface. Since gas velocity in the boundary layer is much lower than that of the mainstream, flow is driven primarily by the pressure gradient and the viscosity of the non slip boundary. Under the intervention of reduced static pressure gradient distributed along blade height and leakage of the tip clearance, the air flow entering from the impeller inlet has a moving trend towards the blade tip direction in the process of developing along the meridional direction. While the air flow near the hub surface is being pushed to the suction side by the wall, the streamline on both sides is climbing to the blade surface under the action of the pressure gradient. When the flow reaches the middle section of the blade, where the radial turning rapidly of the flow channel, the pressure side streamline meets with the suction side streamline along the casing and then begins to flow back to the center of the flow channel, leaving a clear separation line. Meanwhile, gas on the hub surface has increased gradually along the blade height under the centrifugal force until it reach the blade outlet. Because of the continuity, when the gas in the boundary layer generates transverse flow of the vertical channel, the compensation flow will also be generated in the middle of the channel, which will be wound into the passage vortex in the channel.

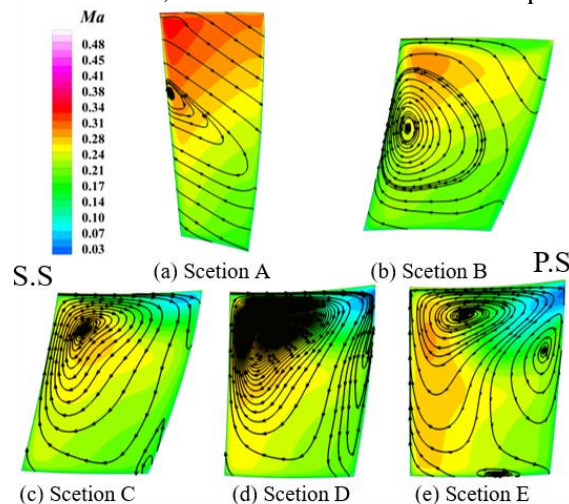


Fig. 9: Sectional streamlines and contours of relative Mach number

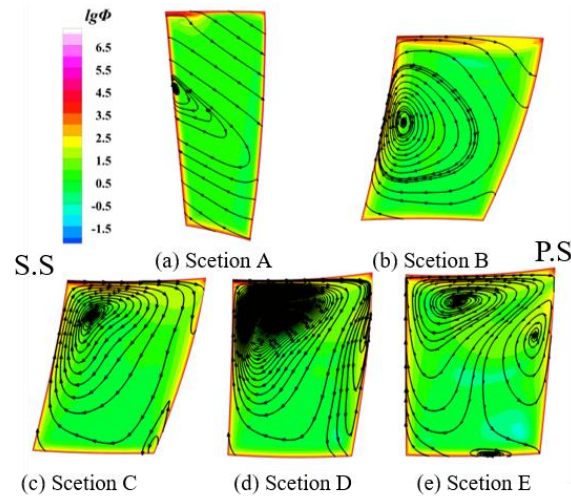


Fig. 10: Sectional streamlines and contours of logarithmic dissipation function

Fig. 9 depicts streamlines drawn by relative velocity and contours of relative Mach number in different flow pass sections under the design condition to observe changes of the passage vortex with the development of the flow. From the figure, the vortex can be divided into the clockwise rotating passage vortex near suction side and the counterclockwise rotating vortex near pressure side. In the sections near the leading edge (Section A and B), the lateral flow near the casing and hub is mainly affected by pressure gradient and wall viscosity effect. Since the passage vortex near suction side matches the movement trend of the impeller, the vortex near the leading edge of the blade rotates clockwise and the vortex core is closer to the suction side. The low-energy fluid in the boundary layer on the pressure side, along with the flow, moves continuously to the blade top under the action of pressure gradient. The compensation flows begin to appear in the 50% flow pass section (Section C) and a pressure driven vortex system is formed in the 70% flow pass section (Section D). By the way, near the outlet section (Section E), small clockwise vortex also appears in the corner between pressure side and hub, whose structure is similar to the vortex driven by stress. In contrast to pressure driven secondary flow, stress driven secondary flow is caused by a fluctuation of turbulent velocity at the wall corner [12]. The air flows out from the wall corner along both sides, then returns to the center of the channel along the edge bisector.

Fig. 10 shows the sectional streamlines and contours of logarithmic dissipation function under the design condition. From the five sections in the figure, it is clear that high dissipation is only distributed within boundary layer near the wall and leakage area at blade tip, but the vortex structure in mainstream area doesn't bring obvious energy loss. The reason is that the energy loss caused by fluid deformation occurs mostly donated by the shear action between the boundary layer and the main stream. There is no obvious velocity difference, which dominates the energy loss, in the passage vortex core formed by compensation. As for the corner between pressure side and casing near the outlet section (Section D and E), the high dissipation caused by flow separation is observed, but the magnitude is still a little lower than the dissipation value in boundary layer and leakage area.

4. Conclusion

In this paper, the flow characteristics inside the NASA LSCC impeller under design condition are studied by RNS method, and the main phenomena and conclusions are as follows:

- (1) The leakage vortex and scraping vortex near the casing are mainly affected by the convection of low-energy fluid near the blade tip and the relative action of blades. The distribution of passage vortex inside blade passage is mainly dominated by pressure, and two counter rotating vortices gradually formed in the flow process.
- (2) The dissipation area of LSCC is mainly reflected in leakage vortex and boundary layer. The scraping vortex only shows the convergence effect of low-energy fluid, which means the flow loss caused by fluid deformation is mainly donated by shear effect of wall and the interaction between leakage vortex and main flow.

- (3) The flow separation in the corner between pressure side and casing also brings high dissipation, but its magnitude is far lower than the dissipation value in boundary layer and leakage area, which indicates that existence of flow separation will also bring flow loss, but it doesn't play a leading role.

Acknowledgements

This study is funded by the NSFC under Grant 51976061.

References

- [1] Brun Klaus, Kurz Rainer. "Analysis of Secondary Flows in Centrifugal Impellers," *International Journal of Rotating Machinery*, 2005, 2005(1):
- [2] M.N.Labib, Woo Ju-sik, Choi Du-youl, T.Utomo, B.Fajar, Chung Han-shik, Jeong Hyo-min. "Numerical assessment on improving multistage centrifugal impeller performance by changing inlet skew angle at impeller inlet," *Journal of Central South University*, 2012, 19(04):953-961.
- [3] Kupferschmied, P., Köppel, P., Gizzi, W., Roduner, C., Gyarmathy, G., 2000. "Time-resolved flow measurements with fast-response aerodynamic probes in turbomachines," *Measurement Science and Technology* 11, 1036–1054.. doi:10.1088/0957-0233/11/7/318
- [4] Johnson, M. W., and Moore, J. (April 1, 1980). "The Development of Wake Flow in a Centrifugal Impeller." *ASME. J. Eng. Power*. April 1980; 102(2): 382–389.
- [5] Kang Shun, Chen Dang-Hui, "Application of CFD in the Investigation of the Secondary Flow in a High Speed Centrifugal Impeller," *Journal of Aerospace Power*, 2005(06):1054-1060. DOI:10.13224/j.cnki.jasp.2005.06.027.
- [6] Xi Guang, Wang Xiao-Feng, Fan Hui-Yuan. "Numerical Study of the Flow Inside the NASA's Low-Speed Centrifugal Compressor Impeller," *Journal of Engineering Thermophysics*, 2001(02):188-191.
- [7] Hathaway M D , Chriss R M , Strazisar A J. "Laser anemometer measurements of the three-dimensional rotor flow field in the NASA low-speed centrifugal compressor," *NASA TP-3257*, 1995.
- [8] Ghenaiet, A., Khalfallah, S., 2019. "Assessment of some stall-onset criteria for centrifugal compressors," *Aerospace Science and Technology* 88, 193–207.. doi:10.1016/j.ast.2018.12.039
- [9] Zhu Cheng-Min, Xin Ding-Ding. "A New Method for Visualizing 3-D Vortices Structures Using Sectional Data," *Acta Aeronautica et Astronautica Sinica*, 2003(03):193-198.
- [10] Kang Da, Zhong Jin-Jun. "Study on Secondary Flow Vortex Structure in High Pressure Ratio Centrifugal Compressor," *Journal of Propulsion Technology*, 2019, 40(10):2243-2251.
- [11] Sanz, GM, & Flack, RD. "Flow Visualization of Secondary Flows in Three Curved Ducts," in *Proceedings of the ASME 1986 International Gas Turbine Conference and Exhibit*. Volume 1: Turbomachinery. Dusseldorf, West Germany. June 8–12, 1986. V001T01A063. ASME.
- [12] Gessner, F. (1973). "The origin of secondary flow in turbulent flow along a corner," *Journal of Fluid Mechanics*, 58(1), 1-25. doi:10.1017/S002211207300